Numerical interpretation of the MARA 10 test simulating a Hypothetical Core Disruptive Accident in a mock-up schematizing a reactor

Marie-France Robbe, Jean-Yves Cariou, Eloi Treille, Michel Lepareux

▶ **To cite this version:**

Marie-France Robbe, Jean-Yves Cariou, Eloi Treille, Michel Lepareux. Numerical interpretation of the MARA 10 test simulating a Hypothetical Core Disruptive Accident in a mock-up schematizing a reactor. International Conference on Numerical Methods in Continuum Mechanics 2000, Sep 2000, Liptovsky Jan, Slovakia. cea-04177361

HAL Id: cea-04177361
https://cea.hal.science/cea-04177361

Submitted on 4 Aug 2023

HAL is a multi-disciplinary open access archive for the deposit and dissemination of scientific research documents, whether they are published or not. The documents may come from teaching and research institutions in France or abroad, or from public or private research centers.

L'archive ouverte pluridisciplinaire **HAL**, est destinée au dépôt et à la diffusion de documents scientifiques de niveau recherche, publiés ou non, émanant des établissements d'enseignement et de recherche français ou étrangers, des laboratoires publics ou privés.

NUMERICAL INTERPRETATION OF THE MARA10 TEST SIMULATING A HYPOTHETICAL CORE DISRUPTIVE ACCIDENT IN A MOCK-UP SCHEMATIZING A REACTOR

M.F. Robbe
CEA Saclay, DRN-DMT-SEMT, 91191 Gif sur Yvette cedex, France
Tel: (33) 1 69 08 87 49, Fax: (33) 1 69 08 52 42, E-mail: mfrobbe@cea.fr

Y. Cariou
Novatome, NVPM, 10 rue Juliette Récamier, 69006 Lyon, France

E. Treille
Socotec Industrie, 1 av. du Parc, 78180 Montigny le Bretonneux, France

M. Lepareux
CEA Saclay, DRN-DMT-SEMT, 91191 Gif sur Yvette cedex, France

Abstract

In case of a Hypothetical Core Disruptive Accident (HCDA) in a Liquid Metal Reactor, the interaction between fuel and liquid sodium creates a high pressure gas bubble in the core. The violent expansion of this bubble loads the vessel and the internal structures, whose deformation is important. The experimental test MARA10 simulates a HCDA in a mock-up schematizing simply the reactor block of a Fast Breeder Reactor. The test-facility is filled with water topped by an air blanket and the explosion is triggered by an explosive charge.

This paper presents a numerical simulation of the test with the CASTEM-PLEXUS code and an analysis of the computed results. In particular, we describe the evolution of the pressure, gas fraction, velocities in the fluid zone, as well as the displacements, stresses and strains of the internal and external structures.

1 INTRODUCTION

In case of a Hypothetical Core Disruptive Accident (HCDA) in a Liquid Metal Reactor, the interaction between fuel and liquid sodium creates a high pressure gas bubble in the core. The violent expansion of this bubble loads the vessel and the internal structures, whose deformation is important.

During the 70s and 80s, the LMFBR integrity was studied with several computer codes validated on experimental data. These experimental programmes were undertaken by several countries and consisted generally in simplified small-scale test-facilities representing reactors: APRICOT [1], FTR and CBR detail scale models [2], STROVA [3], COVA [4,5,6,7,8], WINCON [9] and MARA.

Based on a 1/30 scale model of the Superphenix reactor, the French programme MARA involved ten tests of gradual complexity due to the addition of internal deformable structures:
- MARA 1 and 2 [10] considered a vessel partially filled with water and closed by a rigid roof,
- MARA 4 [11] represented the main core support structures,
- MARA 8 and 9 [12] were closed by a flexible roof,
- MARA 10 [13] included the core support structures (CSS) and a simplified representation of the above core structure (ACS).

The MARS test [14] rested on a 1/20 scale mock-up including all the significant internal components.

A lot of computer codes were used in the world to simulate HCDA. For instance, in the United States, not less than seven codes were available: PISCES 2 DELK [15], REXCO [16], MICE, ICECO, ICEPEL, STRAW and SADCAT [17].

In Europe, several 2D axisymmetric computer codes were used. They were progressively improved in order to be able to perform more realistic HCDA simulations. First, the finite difference SURBOUM code [18], from Belgonucléaire and AWRE-Aldermaston, was capable to model uncompressible fluid and thin shells. It was replaced by the finite difference SEURBNUK code [19] developed by JRC-Ispra and AWRE-Aldermaston, which could model compressible fluids. As the fluid-structure coupling adopted in this code was very simple (separate resolution of the fluid and structure motions), the code was finally coupled to the finite element EURDYN code for the structure calculation [20,21]. The lagrangian finite difference ASTARTE code [22], developed by the ENEA, could compute compressible fluids and thin shells of simple geometry.

In France, two 2D axisymmetric computer codes specialised in HCDA computations were developed by the CEA-Cadarache. The CASSIOPEE code [23] modeled uncompressible fluids with an eulerian description and thin shells with a lagrangian description. It used a weak coupling and rezonings based on the ALE method.

The lagrangian SIRIUS code [24] described fluids and thick structures with the finite difference method and thin structures with the finite element method. The fluid-structure coupling was realised by a slide-line technique and rezonings were performed during calculation because the internal structure presence caused high distortion of the fluid meshes. The SIRIUS code [25,10] was validated on the MARA programme [26,27].

At the end of the 80s, it was preferred to add a specific HCDA sodium-bubble-argon tri-component constitutive law [28] to the general ALE fast dynamics finite element CASTEM-PLEXUS code. The HCDA constitutive law was qualified [29] on the CONT benchmark [30].

In order to demonstrate the CASTEM-PLEXUS capability to predict the behaviour of real reactors [31,32], axisymmetrical computations of the MARA series were confronted with the experimental results. The computations performed at the beginning of the 90s showed a rather good agreement between the experimental and computed results for the MARA 8 and MARA 10 tests even if there were some discrepancies which might be eliminated by increasing the fineness of the mesh [33]. On the contrary, the prediction of the MARS structure displacements and strains was overestimated [34].

As the method used for dealing with the fluid-structure coupling was improved since then, it was undertaken another comparison between the experimental and numerical results and a more detailed analysis of the results. After a brief presentation of the test-facility MARA 10, this paper is focused on the numerical model and the analysis of the results computed by the code CASTEM-PLEXUS.

2 DESCRIPTION OF THE MARA10 TEST-FACILITY

The primary circuit of the Superphenix reactor (Fig. 1) is a "pool" design [35]. The whole core, primary pumps and intermediate heat exchangers are enclosed in the main reactor vessel which is made of stainless steel and welded to the roof slab. The main reactor vessel is encased in a safety vessel also made of stainless steel.

The MARA10 experiment belongs to the MARA test programme defined and realised at the CEA-Cadarache in order to simulate a HCDA in small scale (1/30) mock-up of the Superphenix reactor block. The external dimensions of the MARA10 test are 55 cm high and 35 cm of radius.

The characteristics [33] of the mock-up are:
- a scale factor of 1/30 for all dimensions and thickness,
- an axisymmetrical geometry,
- sodium is represented by water, argon by air and the bubble expansion by an explosive source.

All tests of the MARA series were fired using a 45 g low density low pressure explosive charge of L54/16 composition [36] leading at least to a 1000 MJ full scale energy release [26]. The bare vessels were filled with water leaving a 4.3 cm air gap [12]. All the vessels were identical and made of 316 steel of 1.2 mm thickness, except between the junctions with the core support plate and the internal heat exchangers where the thickness was locally reduced from 0.9 to 1.1 mm in order to simulate a pinned attachment with the core support structure.

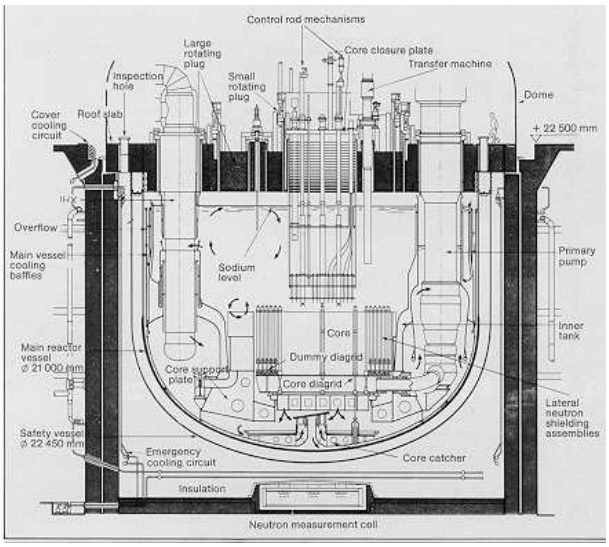

Fig. 1: The Superphenix reactor

In MARA10, a flexible roof of 10 mm thickness A42 steel was clamped to the roof support [12]. The vessel was welded to a flange bolted to the roof support. The MARA10 test-facility (Fig. 2) included the main internal structures [13] of the Superphenix reactor:

- The core support structure (CSS) was machined from a single block of Au4g aluminium. It was supported by a thin collar attached to the vessel base.
- The diagrid was a 304L steel plate of 8.8 mm thickness just resting under gravity on the inner flange of the core support.
- The radial shield was represented by a deformable A316 steel cylindrical vessel of 200 mm diameter. The shield base was welded to a flange, clamped by bolts to the diagrid,
- The above core structure (ACS) was a 1 mm thick deformable A316 cylinder of 140 mm diameter and 210 mm height, completely filled with water to avoid buckling of the wall as a consequence of the deflection of the base (also 1 mm thickness).

The ACS was securely clamped to the deformable roof by bolts. The welded corner between wall and base plate was stiffened to avoid rupture.
The explosive charge was supported at the base of the ACS.

3 NUMERICAL MODELING OF THE TEST-FACILITY

The MARA10 test-facility is composed of structures and fluids interacting with each other. The mock-up is surrounded by a flexible roof and a flexible vessel and contains internal structures: the core support structure fixed to the vessel by a collar, the diagrid, the radial shield and the above core structures. The structures are assumed to be thin enough to be represented by shells except the core support structure which is supposed rigid.

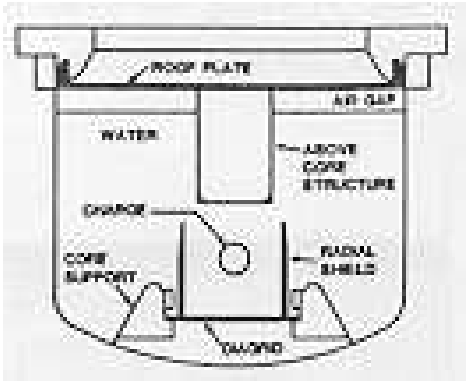

Fig. 2: The MARA10 test-facility

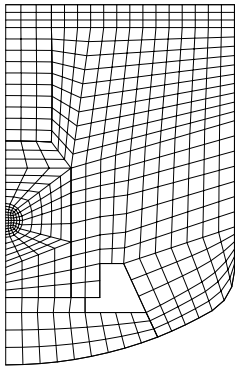

Fig. 3: Mesh of the MARA10 test

In case of a HCDA, the internal fluids are sodium, argon and a gas bubble. In the MARA10 test, these fluids are respectively replaced by water, air and an explosive charge. Water and air were initially at the atmospheric pressure whereas the explosive charge induces an initial pressure of 165 MPa in the bubble area.

CASTEM-PLEXUS [37,38,39,40] is a general fast dynamics finite element code deveoted to the analysis of problems involving fast transients. It can deal with fluids and structures with a possibility of coupling. A specific CDA constitutive law was implemented in the code in order to be able to represent precisely this kind of explosion [41]. The characteristics taken into the numerical model are:

- Water : $\rho = 998.3$ kg/m3 sound speed $C = 1550$ m/s $p^{(0)} = 10^5$ Pa
- Air : $\rho = 1.206$ kg/m3 $\lambda = c_p/c_v = 1.4$ $p^{(0)} = 10^5$ Pa
- Explosive charge : $\rho = 400$ kg/m3 polytropic coef. $\eta = \lambda = 1.24$ $p^{(0)} = 1.646\,10^8$ Pa

Two kinds of fluid-structure coupling are available in the CASTEM-PLEXUS code. Their main differences lie in the definition of the local normal vector used to write the coupling relations between the freedom degrees of the fluid and the solid. The first fluid-structure coupling (FS2D instruction) requires the definition of coupling elements by the user and imposes to the fluid nodes to have the same displacements as the structure nodes. Besides, there is no automatic actualisation of the ALE grid for the elements other than the ones on the coupled lines. The second coupling (FSA instruction) goes without coupling elements; the code considers directly the fluid and solid nodes in contact and writes relations allowing a possible tangential movement of the fluid in relation to the structure. The FSA coupling is well adapted to complex geometries but it often implies a user intervention to pilot the displacements of the fluid ALE grid.

The FSA coupling was adopted for the MARA10 test because the presence of the internal structures involves large local displacements of the fluid grid. However, the user has to govern in some cases the local displacement of the mesh. In the previous CASTEM-PLEXUS computations, the FS2D coupling was used because the FSA coupling was developed later.

Owing to the symmetry of the mock-up, an axisymmetric representation (Fig. 3) was used for the numerical simulation.

The boundary conditions are:
- No horizontal displacement of the structures and fluids on the symmetry axis,
- No rotation of the two vessel and roof nodes located on the symmetry axis,
- Complete blocking of the node in the top corner at the junction between the vessel and the roof,
- No horizontal displacement of the core structure,
- No horizontal displacement and no rotation of the structure nodes located on the symmetry axis (ACS, diagrid, vessel).

4 RESULTS

4.1 Pressure

The figure 4 presents the pressure versus time in the whole mock-up. Initially, the pressure is the atmospheric pressure in all the fluid zone, except in the centre where the bubble pressure is 165 MPa. The pressurised area expands immediately with a spherical shape. The pressure wave impacts the radial shield since 0.04 ms, the diagrid and the base of the Above Core Structure at 0.06 ms.

The pressure wave continues its spherical progression. The Core Support Structure is impacted at 0.1 ms. From that time, the pressure in the centre starts decreasing. The pressure wave hits the vessel bottom at 0.14 ms. The average pressure in the pressurised zone decreases in proportion with the volume of the zone. The highest pressure is located in the lower part of the cylinder composed by the diagrid and the radial shield.

From 0.18 to 0.22 ms, the pressure wave propagates in the whole liquid water zone. As the vessel prevents a downward progression, the pressure wave propagates laterally towards the lateral wall of the vessel. The pressure wave impacts the lateral wall of the vessel at 0.22 ms. A depressurised zone forms on the outer side of the radial shield. Progressively, the pressure decreases in the area between the vessel base and the diagrid.

The pressure wave impacts the ACS top at 0.2 ms by propagating vertically in the water contained into the ACS. Out of the ACS, the pressure wave is absorbed by the compression of the air layer located below the roof and around the ACS. In the air zone, the pressure stays at the atmospheric pressure until 1 ms. At 0.22 ms, we still notice a high pressure of about 20 MPa in the central area because of the confinement imposed by the proximity of the radial shield, the diagrid and the ACS bottom.

From 0.26 ms, the pressure globally decreases in the whole test-facility. At 0.26 ms, a pressurised zone is still existing near the lateral wall of the vessel because the pressure wave continues arriving from the centre. Later, a pressure of about 5 MPa persists against the vessel. The pressure in the ACS and in the initial bubble zone is slower to decrease: both areas are still pressurised at 1 ms. Globally, the highest pressure remains located in the central zone all along the computation because the confinement provided by the surrounding structures hampers the exhaust of the central pressurised fluid.

4.2 Gas fraction

The figures 5 to 7 show respectively the general volumic presence fraction of the gas, the massic presence fractions of the bubble and of the air. Initially, the gas is located in the centre of the mock-up and under the roof. The ACS is completely filled with liquid water. Between 0.04 and 0.2 ms, we observe an expansion of the central bubble (simulating the explosive charge) which stays inside the central zone. The air layer remains unchanged.

From 0.5 ms, water vaporises out of the radial shield, below the diagrid, along the ACS lateral wall and at the limit with the air layer. This vaporisation occurs after the passing of the pressure wave, during the depressurisation phase. The air layer is also compressed against the roof by the water propelled upwards.

At 1 ms, the bubble gas starts escaping from the central zone, confined by the proximity of the three following structures: radial shield, diagrid, ACS base. It goes away by the free space between the shield and the ACS. The air is still more compressed upwards and pushed towards the top corner but an air film remains always present under the whole roof.

Between 1.4 and 2.4 ms, the steam zone below the diagrid desappears progressively. At 2.4 ms, the steam zone surrounding the radial shield reaches its maximum extension. From 2 ms, the air zone stops reducing and starts expanding under the roof. In the central zone, the bubble gas is no more located in the centre; it had gone up and the upper part of the central zone is almost entirely gaseous.

Between 3 and 6 ms, the bubble gas continues escaping from the central zone and going up towards the roof. The steam layer around the radial shield decreases progressively; a steam bag remains present between the core support structure and the shield. A diphasic water film forms next to the vessel base: it appears first near the symmetry axis and extends to whole base. The water at the top of the ACS and then above the ACS base vaporises according to the pressure wave reflections in the structure. The air layer around the ACS becomes larger.

Between 7 and 9 ms, the steam in the lower part of the mock-up condenses progressively; the last diphasic zone is located near the CSS. The bubble continues its expansion out of the central zone. The steam in the ACS spreads out. The air zone extends along the ACS in the initial water zone.

4.3 Fluid velocity

The figures 8 and 9 show the fluid velocities with vectors to indicate the fluid direction and with a colour map to give an idea of the value of the velocities. The fluid is initially at rest in the whole test-facility.

At 0.02 ms, the fluid is expelled from the central zone in all the directions with a speed independent from the direction and worthing about 200 m/s.

At 0.1 ms, the highest speeds are located in the central zone again but the velocities are no more uniform. Their value is around 140 m/s. Owing to the diagrid presence and the radial shield, the downward velocities are lower than the radial ones, themselves lower than the diagonal ones. The upward velocities of the central zone have a reduced value compared with the diagonal ones, because of the ACS base presence. But the speeds on the symmetry axis are an exception. Out of the central zone, the fluid starts moving too: particularly near the radial shield where the fluid goes towards the lateral wall.

At 0.18 ms, we observe a rise of the velocities on the symmetry axis: they reach 250 m/s. In the central zone, the downwards velocities have a reduced value while the radial speeds and diagonal ones are around 80 m/s. The fluid escapes by the narrow opening between the radial shield top and the ACS base what explains those high speed values. Out of the central zone, the fluid is globally ejected spherically except near the CSS where the fluid goes round the obstacle. At that time, the fluid impacts the vessel base with a perpendicular speed.

From 0.3 to 0.5 ms, the whole fluid is moving. The highest speeds are registered again for the fluid escaping between the shield and the ACS. The water impacts the vessel bottom almost vertically with a speed of 50 m/s. The roof is impacted with speeds decreasing from 40 m/s in the centre to almost zero at the edge. In the upper part of the mock-up, the velocities are oriented upwards. Out of the central zone and at the horizontal level of the radial shield, the velocities are mainly directed horizontally and the fluid impacts the lateral wall perpendicularly. In the bottom corner, the fluid first impacts the vessel and then is pushed away from the corner and it impacts once again the vessel but just above the bottom corner or at the junction of the vessel and the collar.

Between 0.8 and 1.2 ms, we observe the same phenomena except in the vicinity of the lower part of the lateral wall where the velocities decrease.

Between 1.6 and 3.2 ms, the velocities decrease in the central zone, apart from the water going out by the free space between the shield and the ACS: locally the speed is still of 70 m/s. In the ACS, the upwards speed decreases and we observe a downward flow reversal after the impact of water against the roof. In the upper zone out of the ACS, the water goes up and the air is pushed upwards and horizontally towards the top corner. In the lower part of the mock-up (half-way down), the speed decreases. It decreases first near the lateral wall and below the diagrid. Because of the proximity of the structures and the confinement they impose to the fluid, we still observe downward fluid movements below the CSS and rebounds between the bottom corner of the vessel and the collar.

At 4 ms, the fluid impacts the lateral wall, just below the roof, with horizontal outwards speeds. Between 4 and 6 ms, the highest speeds are measured again for the fluid going out from the central zone. In that zone, all the fluid movements are oriented upwards, except just below the ACS. Below the diagrid and the CSS, the water is captive of this closed space and rebounds against the structures. In the bottom corner, the water rebounds between the collar and the lateral wall of the vessel. Just above this level, the water moves up. Above the CSS, the water moves towards the radial shield after it was pushed back by the lateral wall.

In the ACS, water alternates up and down flows due to the bounces against the top and the bottom of the ACS. At the level of the ACS but out of them, we note a downward fluid flow along the ACS,

another downward flow along the lateral wall and an horizontal between both zones. Because of the general convergence of water towards the radial shield top, a large whirlpool creates in that area.

From 7 ms, the whirlpool governs the majority of the fluid flows in the mock-up. It sucks the fluid near the lateral wall by means of downward flows near the roof and central directed flows half-way up the lateral wall. These fluids movements impose downward flows of the water below this zone. In particular, water is sent to the nook between the CSS and the shield. The whirlpool also attracts down fluid from the zone below the roof and near the ACS. The whirlpool repulses the water which tries to escape from the central zone.

4.4 Deformed shape

The deformed shape is displayed on the figure 10. At 0.2 ms, we observe structure deformations in the central zone: the ACS bottom buckles and the diagrid centre goes down under the overpressure imposed by the explosive charge. The radial shield top moves away to let escape the fluid out of the central zone. The vessel base moves down because of the impact of the pressure wave.

Between 0.4 and 3 ms, the previous deformations become more pronounced. Besides, the top of the ACS buckle too because of the upward impact of the water inside the ACS. The roof moves up starting from the centre under the impact of the upwards water flows in the upper part of the mock-up. A lower bulge forms in the lateral wall due to the horizontal and then upward fluid flows along the wall.

From 3.8 ms, the ACS base bending reverses because of the downward water flow. All the other deformations remain present. Moreover an upper bulge creates in upper part of the lateral wall due to the local water impact perpendicularly to the wall at 4 ms.

4.5 Radial displacements of the structures

The figure 11 shows the radial displacements of the structures. Since 0.2 ms, the top of the radial shield moves away under the pressurisation caused by the explosive charge.

The radial shield reaches a maximum radial displacement of 12 mm at 0.4 ms. Between 0.4 and 1 ms, the lower part and then almost all the lateral wall of the ACS moves away because of the ACS buckling; the radial displacement remains limited to 2 mm. The lower part of the vessel lateral wall moves away progressively, thus creating a lower bulge. This displacement is smaller than 4 mm. The bottom corner moves laterally but towards the centre because the bottom of the lateral wall is pulled down by the vessel base. The CSS and the collar do not move laterally because the CSS is rigid.

Between 1.4 and 3.2 ms, the radial displacements of the radial shield, of the ACS lateral wall and of the vessel lower bulge remain constant. The displacement of the bottom corner increases and reaches a maximum value of -12 mm. The part of the vessel base half-way between the symmetry axis and the collar attachment moves slightly away because of the rebounds of the water captive below the diagrid and the CSS. At the vessel-collar junction, the vessel remains fixed because the CSS prevents all the lateral motions.

Between 4 and 6 ms, besides the previous displacements, a new radial displacement appears in the upper part of the lateral wall of the vessel. The maximum displacement of this upper bulge is 10 mm at 5 ms.

From 7 ms, the ACS buckling and the upper bulge decrease. The lower bulge, the radial shield gap and the bottom corner pulling stay identical. The bottom vessel radial deformation moves laterally according to the position of the fluid impacting the vessel in the course of its rebounds.

4.6 Vertical displacements of the structures

The figure 12 presents the vertical displacements of the structures. During the first 0.2 ms, the diagrid centre starts falling down because of the overpressure imposed by the explosive load. The radial shield goes down because the outward motion of the structure also implies a slight going down.

At 0.4 ms, the vessel base between the centre and the collar attachment moves down. The complete diagrid and the radial shield continue going down. The ACS base starts moving up thus inducing an ACS buckling.

At 0.6 ms, the upward motion of the ACS base goes on and it also imposes the going up of the lower part of the ACS lateral wall. The vessel bottom continues going down what pulls down the complete set of the below core structures (core support structure, collar, diagrid, radial shield).

Between 0.8 and 2.2 ms, the downward motion of the vessel and of the below core structures progresses; it reaches a maximum fall of 35 mm at 2.2 ms. Simultaneously, the upwards movement of the ACS base propagates to the whole ACS at 0.8 ms. Later the ACS upward motion pulls up the roof part next to the ACS. The maximum ACS displacement is reached at 2.2 ms: 35 mm up for the ACS bottom and 20 mm for the ACS top.

Between 3 and 5 ms, the downward displacement of the lower part of the mock-up decreases a little. Simultaneously, the ACS bottom moves down back (reversal of the curvature direction of the ACS base) while the ACS top continues moving up because of the up and down water flows inside the ACS. The ACS top reaches a maximum upward displacement of 25 mm at 5 ms. This upward motion pulls a bit more the roof and a larger roof zone is concerned by the upward motion.

From 6 ms, the bottom vessel and the below core structures remain at the same location. On the contrary, the displacements of the ACS and the roof decrease; both structures come back.

4.7 Von Mises stresses in the structures

The figure 13 shows the stresses in the external and internal structures. The first stress location appears in the radial shield since 0.06 ms. Between 0.08 and 0.16 ms, stresses progress in the whole radial shield, the connection with the diagrid and then the diagrid. The junction between the shield and the CSS is very much in demand. Simultaneously, stresses appear in the ACS bottom and extend up to the whole lateral wall of the ACS.

Between 0.16 and 0.22 ms, the stresses become higher in the previous quoted places. Besides, the collar attaching the vessel to the CSS is put under stress and the stresses propagate to the whole vessel bottom from that point. The junction between the ACS top and the roof is also in demand.

From 0.26 to 0.5 ms, the stress level increases in the radial shield and its junction with the CSS. The stresses reaches a maximum of 700 MPa at the shield top and 850 MPa at the junction with the CSS at 0.5 ms. The stress level also increases in the vessel bottom. The stresses go up progressively in the vessel lateral wall because of the constitution of the lower bulge: their average level is around 400 MPa.

Several spots of high stress (up to 1000 MPa) appear in the proximity of the bottom corner. Those spots are due to the corner presence and to the vessel thickness changes in that area. The stress level increases in the collar and the extremity of the CSS; it reaches approximately 350 MPa. The CSS being rigid, the stress level never changes. The stresses also rise in the ACS; a maximum of 500 MPa in the ACS lateral wall is obtained at 0.5 ms. The ACS top begins to be in demand as well as the neighbouring part of the roof.

Between 1 and 3 ms, the stresses decrease in the diagrid, in the lateral wall of the vessel, in the collar and in the radial shield. On the contrary, the stresses increase in the bottom corner; they reach a maximum of 900 MPa in the corner from 1 to 2 ms. The junction between the collar and the vessel stays a location very much in demand until the end of the computation.

In the ACS, the stresses increase and decrease alternatively according to the rebounds of water on both extremities of the component. At the centre of the ACS bottom, a stress of 600 MPa is measured at 1 ms. The stresses increase in the entire roof until 1.6 ms when they reach a maximum value of 250 MPa. Afterwards, the stress level decreases in the roof.

From 5 to 9 ms, we observe a general fall of the stress level in all the structures. The mere point to remain at a high level of stress until the end is the attachment of the collar on the vessel.

4.8 Plastic strains of the structures

The figure 14 show the plastic strains versus time. The mock-up structures remain elastic for the first 0.1 ms. At 0.16 ms, the ACS base and the top of the radial shield become slightly plastic. From 0.26 to 0.6 ms, the plasticity level increases in the radial shield, the ACS base and lateral wall. Plastic deformations appear in the diagrid and at the bottom of the vessel near the symmetry axis.

Between 1.2 and 3 ms, the plastic level increases in all the parts of the structures already quoted. In particular, the plastic strains reach 13 % at the top of the radial shield, 3 % in the diagrid and 4 % on the vessel base. A new plastic zone is created in the bottom corner.

At 4 ms, the plastic strains in the ACS base reach a maximum of 7 %. Between 4 and 6 ms, a last plastic zone forms in the upper part of the vessel because of the formation of the upper bulge. In that area, the strains remain limited to 2 %. From 7 to 9 ms, the plastic strains remain identical in the whole test-facility.

5 CONCLUSION

In that paper, we present a computation of a Hypothetical Core Disruptive Accident in the MARA10 test-facility representing a simplified geometry of a reactor. This mock-up contains the main internal structures of the reactor block of a Liquid Metal Fast Breeder Reactor. The fluids intervening in the real accident were replaced by water, air and an explosive charge in the experiment.

In the numerical model, the structures are represented by shells. The internal fluids are described by the specific CDA constitutive law implemented on purpose in the CASTEM-PLEXUS code for computing this kind of explosion. The CASTEM-PLEXUS code succeeded in carrying out the computation of the explosion until 9 ms of physical time.

The explosive charge in the centre causes the propagation of a pressure wave which impacts first the radial shield, the diagrid and the Above Core Structure base and later the vessel bottom and vessel lateral wall and finally the roof.

The bubble gas expands in the central zone confined by the internal structures and afterwards it escapes in the rest of the mock-up by the narrow space between the ACS and the shield. Water vaporises out of the radial shield, below the diagrid and in the ACS. The air layer is compressed under the roof by the water pushed upwards by the explosion.

Very soon, the diagrid moves down, the radial shield goes away and the ACS base goes up. Then the vessel base moves down and the lateral wall goes away, thus creating a lower bulge. The ACS lateral wall buckles, the ACS top goes up, thus pulling up the rest of the roof. Finally, an upper bulge creates in the upper part of the vessel lateral wall and the ACS base changes curvature.

For the last test of the MARA series (MARS test), specific developments for testing the influence of the internal structures were realised in the CASTEM-PLEXUS code. This mock-up contains, besides a more precise description of the internal structures present in the MARA10 test, a set of structures representing the heat exchangers and the pumps. These structures have a far too complex geometry to mesh them. Consequently, a model [42,43] was developed to homogenize the structures with the surrounding fluid and to take into account their presence simply.

REFERENCES

[1] West, P.H., Hoskin, N.E. APRICOT - Phase 3. Suggested simple test problems for examination of thin shell modelling and fluid structure coupling, Aldermaston report AWRE/44/92/16, 1980. [2] Cagliostro, D.J., Florence, A.L., Abrahamson, G.R., 1979. Scale modeling in LMFBR safety, Nuclear Engineering and Design 55, 235-247.

[3] Kendall, K.C., Adnams, D.J., 1986. Experiments to validate structural dynamics code used in fast reactor safety assessment, Science and Technology of Fast Reactor Safety, Vol. 2, British Nuclear Energy Society, London, England.
[4] Hoskin, N.E., Lancefield, M.J., 1978. The COVA programme for the validation of computer codes for fast reactor containment studies, Nuclear Engineering and Design 46, 17-46.
[5] Holtbecker, H., 1977. Testing philosophy and simulation techniques, Nuclear Engineering and Design 42, 75-87.
[6] Albertini, C., et al. The JRC-COVA programme : Final Report. Commission of the European Communities, Report EUR 8705, 1983. Nuclear Science and Technology, 1984, pp. 1-182.
[7] Wenger, H.U., Smith, B.L., 1987. On the origin of the discrepancies between theory and experiment in the COVA series, Proc. 9th Int. Conf. on Structural Mechanics In Reactor Technology, Vol. E, Lausanne, Switzerland, pp. 339-344.
[8] Kendall, K.C., Benuzzi, A., 1980. The COVA programme : Validation of the fast reactor containment code SEURB-NUK, Nuclear Engineering and Design 57, 79-105.
[9] Sidoli, J.E.A., Kendall, K.C. The WINCON programme - Validation of the fast reactor primary containment codes. Proc. INE Int. Conf. On Nuclear Containment, Cambridge, England, April 1987. Nuclear Containment Structures, D.G. Walton, Cambridge University Press, 1988.
[10] Acker, D., Benuzzi, A., Yerkess, A., Louvet, J., August 1981. MARA 01/02 - Experimental validation of the SEURB-NUK and SIRIUS containment codes, Proc. 6th Int. Conf. on Structural Mechanics In Reactor Technology, Section E 3/6, Paris, France.
[11] Smith, B.L., Fiche, C., Louvet, J., Zucchini, A., August 1985. A code comparison exercise based on the LMFBR containment experiment MARA-04. Proc. 8th Int. Conf. on Structural Mechanics In Reactor Technology, Section E 4/7, Brussels, Belgium, pp. 151-157.
[12] Fiche, C., Louvet, J., Smith, B.L., Zucchini, A., August 1985. Theoretical experimental study of flexible roof effects in an HCDA's simulation, Proc. 8th Int. Conf. on Structural Integrity In Reactor Technology, Section E 4/5, Brussels, Belgium, pp. 139-144.
[13] Louvet, J., Hamon, P., Smith, B.L., Zucchini, A., August 1987. MARA 10: an integral model experiment in support of LMFBR containment analysis, Proc. 9th Int. Conf. on Structural Mechanics In Reactor Integrity, Section E, Lausanne, Switzerland, pp. 331-337.
[14] Falgayrettes, M., Fiche, C., Granet, P., Hamon, P., Barrau, P., Magnon, B., Jalouneix, J., Nédélec, M., 1983. Response of a 1/20 scale mock-up of the Superphenix breeder reactor to an HCDA loading simulation, Proc. 7th Int. Conf. on Structural Mechanics In Reactor Technology, Section E 4/1, Chicago, USA, pp. 157-166.
[15] Cowler, M.S., Hancock, S.L., 1979. Dynamic fluid-structure analysis of shells using the PISCES 2 DELK computer code, Proc. 5th Int. Conf. on Structural Mechanics In Reactor Technology, Section B 1/6, Berlin, Germany.
[16] Chang, Y.W., Gvildys, J., Fistedis, S.H., 1974. Analysis of the primary containment response using a hydrodynamic-elastic-plastic computer code, Nuclear Engineering and Design 27, 155-175.
[17] Chang, Y.W., 1977. Application of containment codes to LMFBRs in the United States, Nuclear Engineering and Design 42, 53-67.
[18] Stiévenart, M., Bouffioux, P., Eglème, M., Fabry, J.P., Lamotte, H. August 1975. Analysis of LMFBR explosion model experiments by means of the Surboum-II code, Proc. 3rd Int. Conf. on Structural Mechanics In Reactor Technology, Section E 3/5, London, England.
[19] Cameron, I.G., Hankin, B.C., Warham, A.G.P., Benuzzi, A., Yerkess, A., August 1977. The computer code SEURBNUK-2 for fast reactor explosion containment safety studies, Proc. 4th Int. Conf. on Structural Mechanics In Reactor Technology, Section B 2/1, San Francisco, USA.
[20] Smith, B.L., Yerkess, A., Adamson, J., August 1983. Status of coupled fluid-structure dynamics code SEURBNUK, Proc. 7th Int. Conf. on Structural Mechanics In Reactor Technology, Section B 9/1, Chicago, USA.
[21] Smith B.L., Yerkess, A., Washby, V., August 1987. The computer code SEURBNUK-EURDYN: First release version, Proc. 9th Int. Conf. on Structural Mechanics In Reactor Technology, Lausanne, Switzerland.
[22] Cigarini, M., Daneri, A., Toselli, G., August 1983. Applications of ASTARTE-4 code to explosive models with complex internal structure using the rezoning facility, Proc. 7th Int. Conf. on Structural Mechanics In Reactor Technology, Section B 9/3, Chicago, USA.
[23] Graveleau, J.L., Louvet, P., August 1979. Calculation of fluid-structure interaction for reactor safety with the CAS-

SIOPEE code, Proc. 5th Int. Conf. on Structural Mechanics In Reactor Technology, Section B 1/7, Berlin, Germany.
[24] Blanchet, Y., Obry, P., Louvet, J., August 1981. Treatment of fluid-structure interaction with the SIRIUS computer code, Proc. 6th Int. Conf. on Structural Mechanics In Reactor Technology, Section B 8/8, Paris, France.
[25] Daneri, A., Toselli, G., Trombetti, T., Blanchet, Y., Louvet, J., Obry, P, August 1981. Influence of the representation models of the stress-strain law on the LMFBR structures in an HCDA, Proc. 6th Int. Conf. on Structural Integrity In Reactor Technology, Section E 4/4, Paris, France.
[26] Louvet., J., August 1989. Containment response to a core energy release. Main experimental and theorical issues - Future trends, Proc. 10th Int. Conf. on Structural Mechanics In Reactor Integrity, Vol. E, Anaheim, pp. 305-310.
[27] Bour, C., Spérandio, M., Louvet, J., Rieg, C., August 1989. LMFBR's core disruptive accident. Mechanical study of the reactor block, Proc. 10th Int. Conf. on Structural Mechanics In Reactor Technology, Vol. E, Anaheim, pp. 281-287.
[28] Lepareux, M., Bung, H., Combescure, A., Aguilar, J., August 1991. Analysis of a CDA in a LMFBR with a multiphasic and multicomponent behaviour law, Proc. 11th Int. Conf. on Structural Mechanics In Reactor Integrity, Section E 13/1, Tokyo, Japan, pp. 371-376.
[29] Casadei, F., Daneri, A., Toselli, G., August 1989. Use of PLEXUS as a LMFBR primary containment code for the CONT benchmark problem, Proc. 10th Int. Conf. on Structural Mechanics In Reactor Technology, Section E 13/1, Anaheim, pp. 299-304.
[30] Benuzzi, A., 1987. Comparison of different LMFBR primary containment codes applied to a benchmark problem, Nuclear Engineering and Design 100, 239-249.
[31] Lepareux, M., Bung, H., Combescure, A., Aguilar, J., Flobert, J.F., August 1993. Analysis of an HCDA in a fast reactor with a multiphase and multicomponent behavior law, Proc. 12th Int. Conf. on Structural Mechanics In Reactor Integrity, Section E 7/2, Stuttgart, Germany, pp. 197-202.
[32] Cariou, Y., Pirus, J.P., Avallet, C., August 1997. LMR large accident analysis method, Proc. 14th Int. Conf. on Structural Mechanics In Reactor Technology, Section P 3/7, Lyon, France, pp. 395-402.
[33] Cariou, Y., Spérandio, M., Lepareux, M., Christodoulou, K., August 1993. LMFBR's whole core accident. Validation of the PLEXUS code by comparison with MARA tests, Proc. 12th Int. Conf. on Structural Mechanics In Reactor Technology, Section E 7/4, Stuttgart, Germany.
[34] Cariou, Y., Lepareux, M., Noé, H., August 1997. LMR's whole core accident. Validation of the PLEXUS code by comparison with MARS test, Proc. 14th Int. Conf. on Structural Mechanics In Reactor Technology, Section P 2/6, Lyon, France, pp. 339-346.
[35] NERSA, 1987. The Creys-Malville power plant, Electricité de France, Direction de l'équipement, Région d'équipement Alpes-Lyon, France.
[36] David, F., 1978. Etude d'une composition explosive flegmatisée. Applications à la déformation d'une cuve, Proc. Symposium sur les hautes pressions dynamiques, Paris, France.
[37] Chavant, C., Hoffmann, A., Verpeaux, P., Dubois, J., 1979. Plexus: A general computer code for explicit Lagrangian computation, Proc. 5th Int. Conf. on Structural Integrity In Reactor Technology, Section B 2/8, Berlin, Germany.
[38] Hoffmann, A., Lepareux, M., Schwab, B., Bung, H., 1984. Plexus - A general computer program for fast dynamic analysis, Proc. Conference on Structural Analysis and Design on Nuclear Power Plant, Porto Alegre, Brazil.
[39] Robbe, M.F., Lepareux, M., Bung, H. Plexus - Notice théorique, CEA report DMT/94-490, 1994.
[40] Robbe, M.F., Galon, P., Yuritzinn, T., November 1999. Castem-Plexus: Un logiciel de dynamique rapide pour évaluer l'intégrité des structures en cas d'accident, Proc. 4th Conf. INSTRUC, Courbevoie, France.
[41] Robbe, M.F., Cariou, Y., Lepareux, M., Treille, E., September 2000. Numerical simulation of a Hypothetical Core Disruptive Accident in the MARA8 mock-up with the CASTEM-PLEXUS computer code, Int. Conf. on Numerical Methods in Continuum Mechanics 2000, Liptovský Ján, Slovak Republic.
[42] Robbe, M.F., August 1999. A porosity method to model the internal structures of a reactor vessel, Proc. 15th Int. Conf. on Structural Mechanics In Reactor Technology, Vol. B, Seoul, Korea.
[43] Robbe, M.F., Bliard, F., April 1999. A porosity model to represent the influence of structures on a fluid flow. Application to a hypothetical core disruptive accident, Proc. 7th Int. Conf. On Nuclear Engineering, paper 7819, Tokyo, Japan.

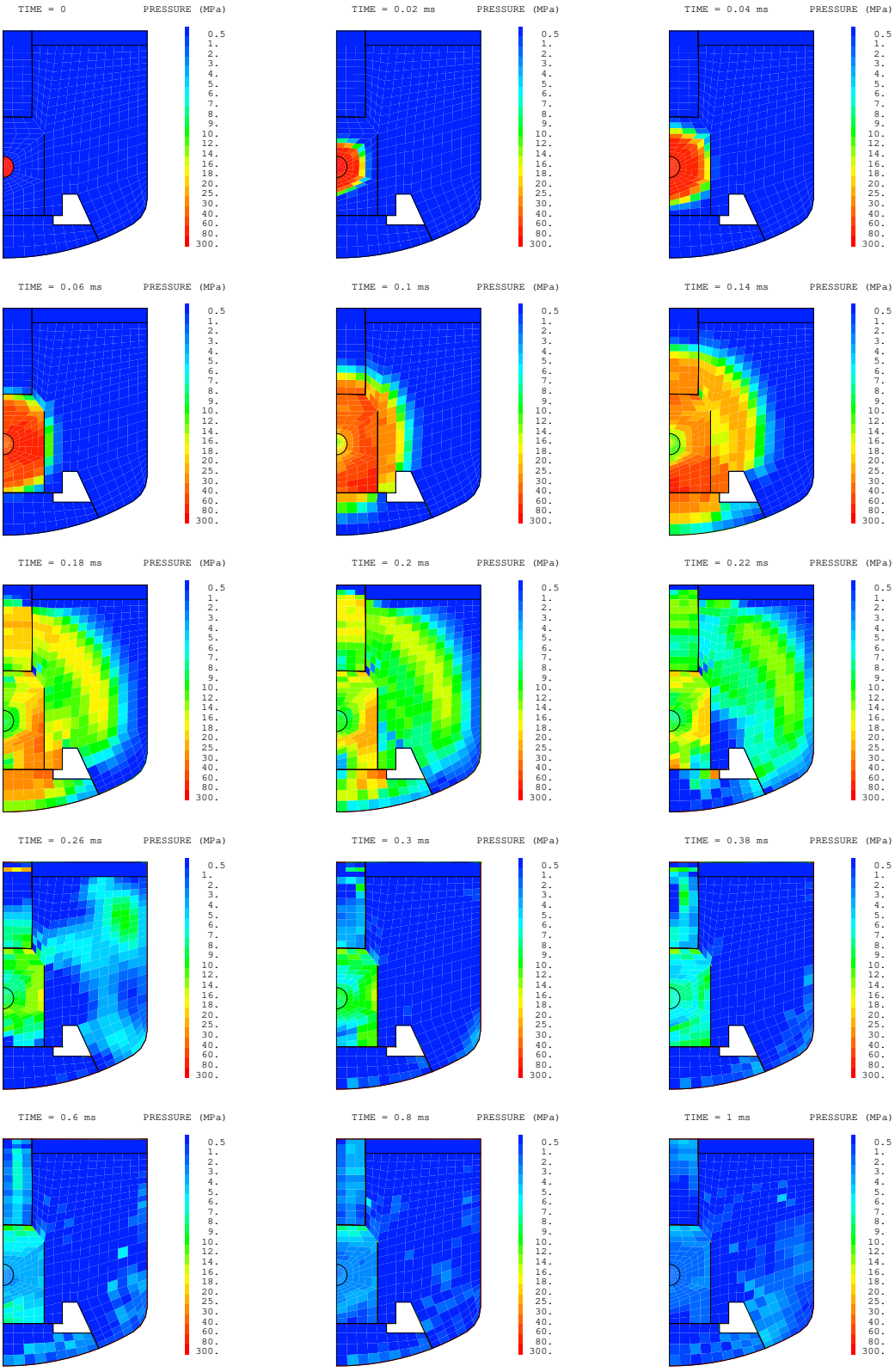

Fig. 4: Pressure

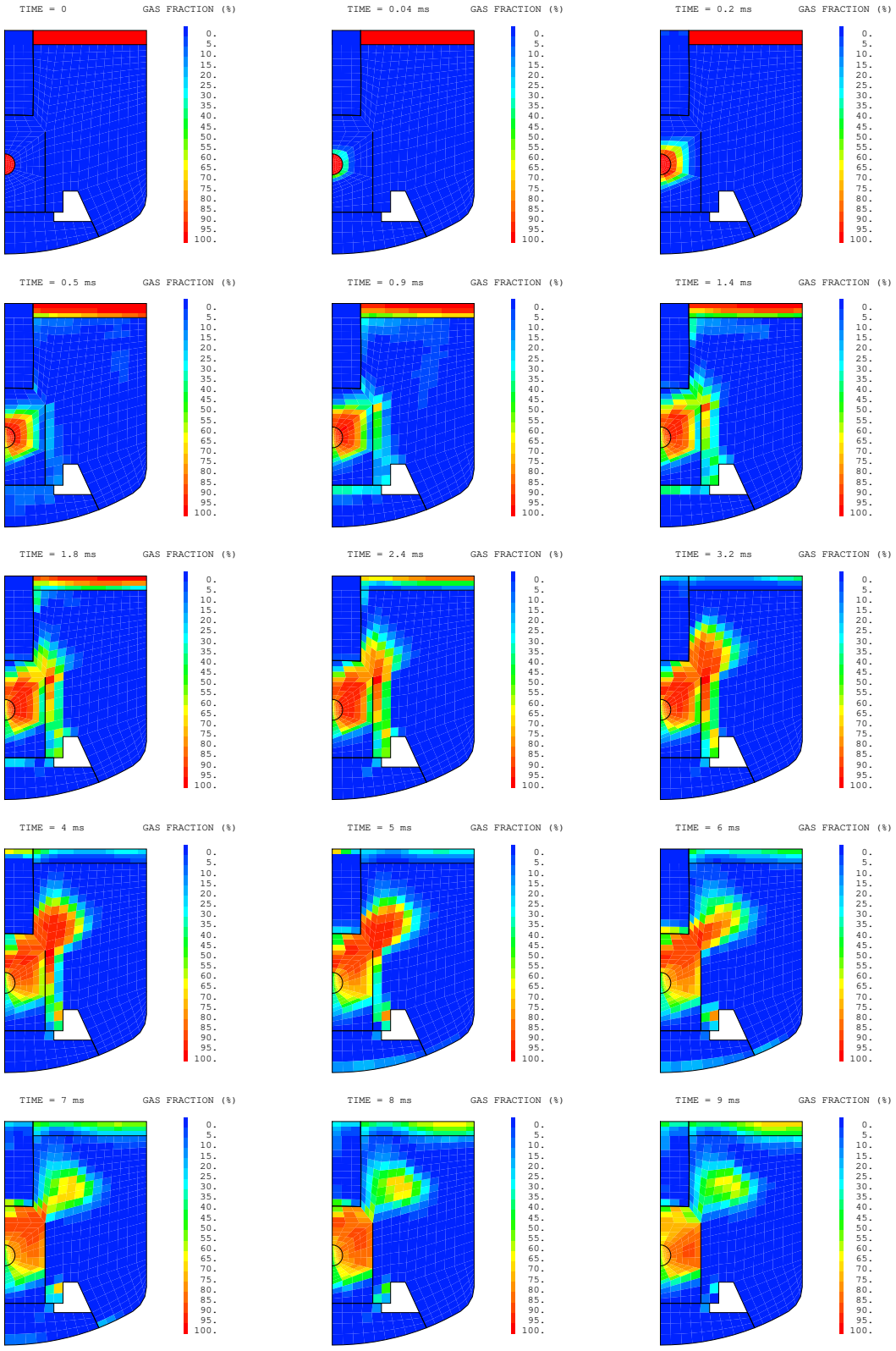

Fig. 5: Gas fraction

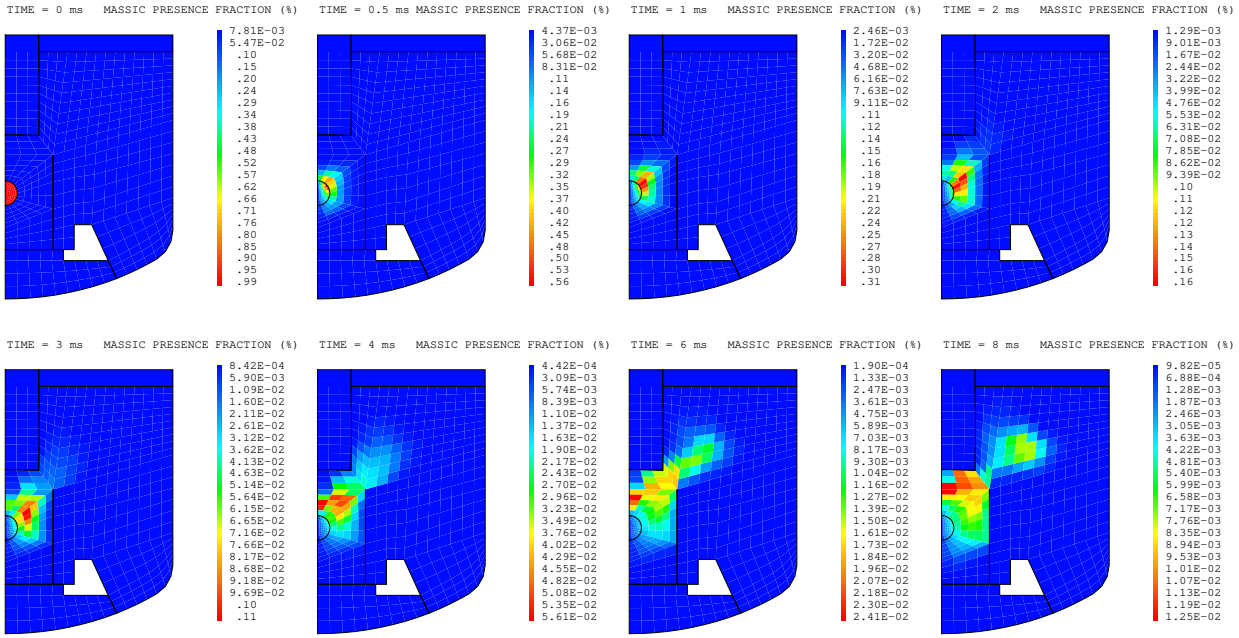

Fig. 6: Bubble massic presence fraction

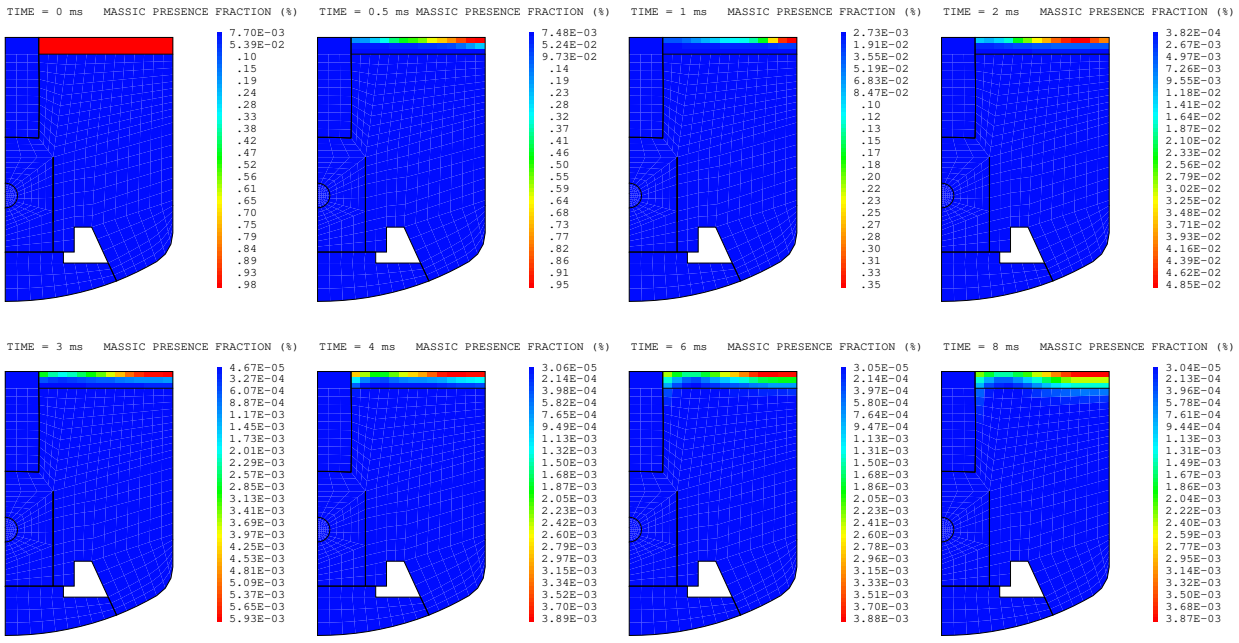

Fig. 7: Air massic presence fraction

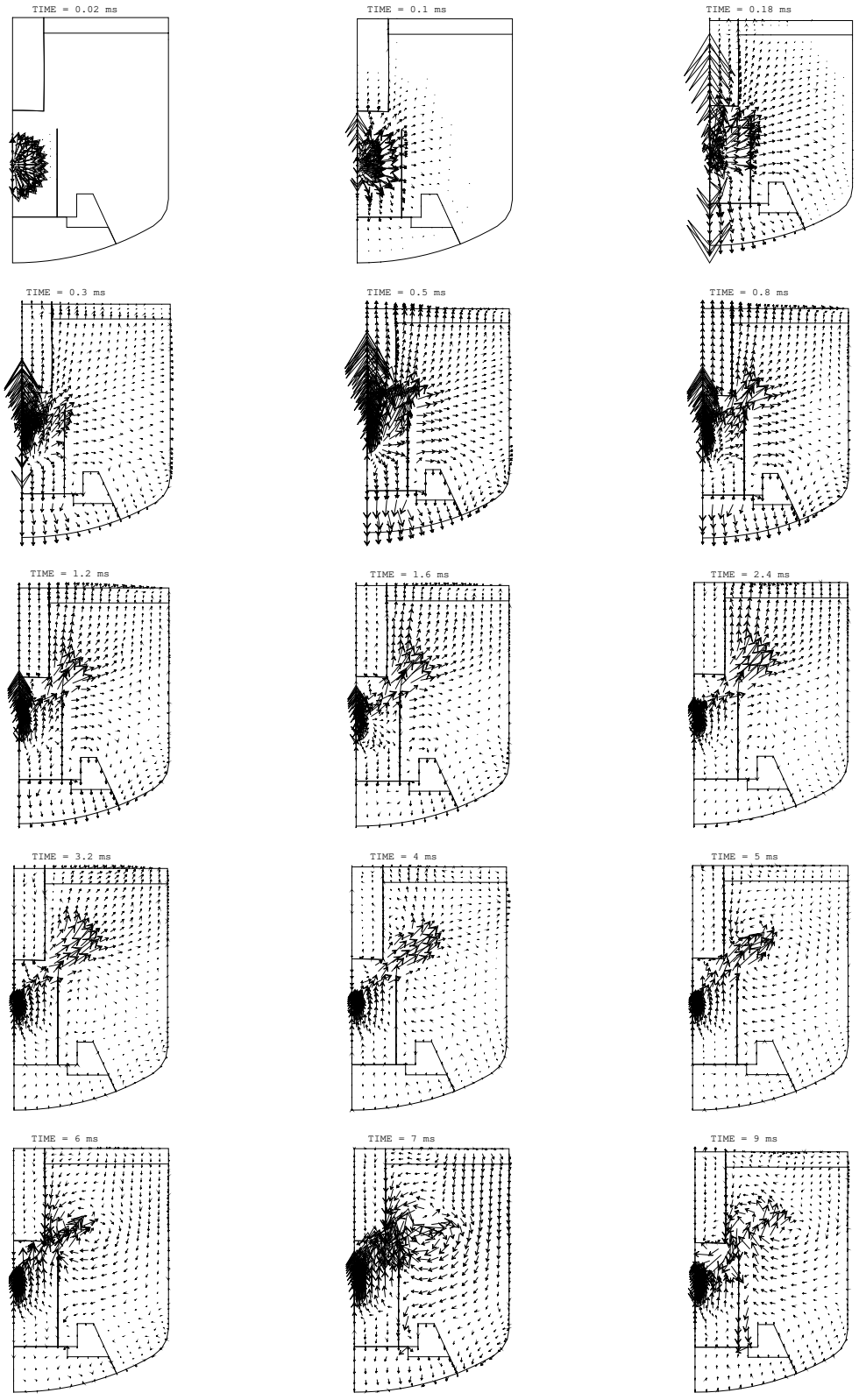

Fig. 8: Fluid speed

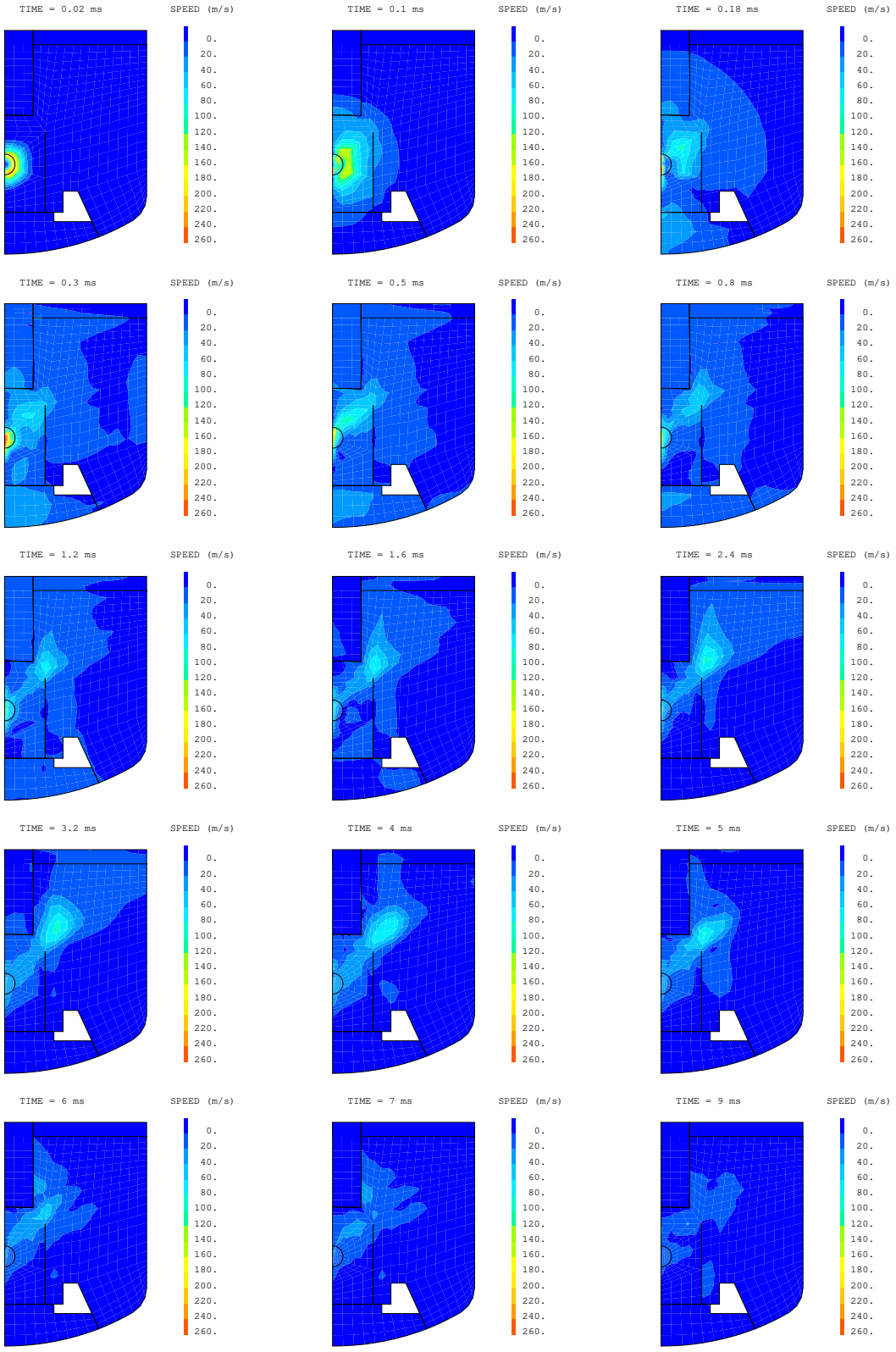

Fig. 9: Fluid speed

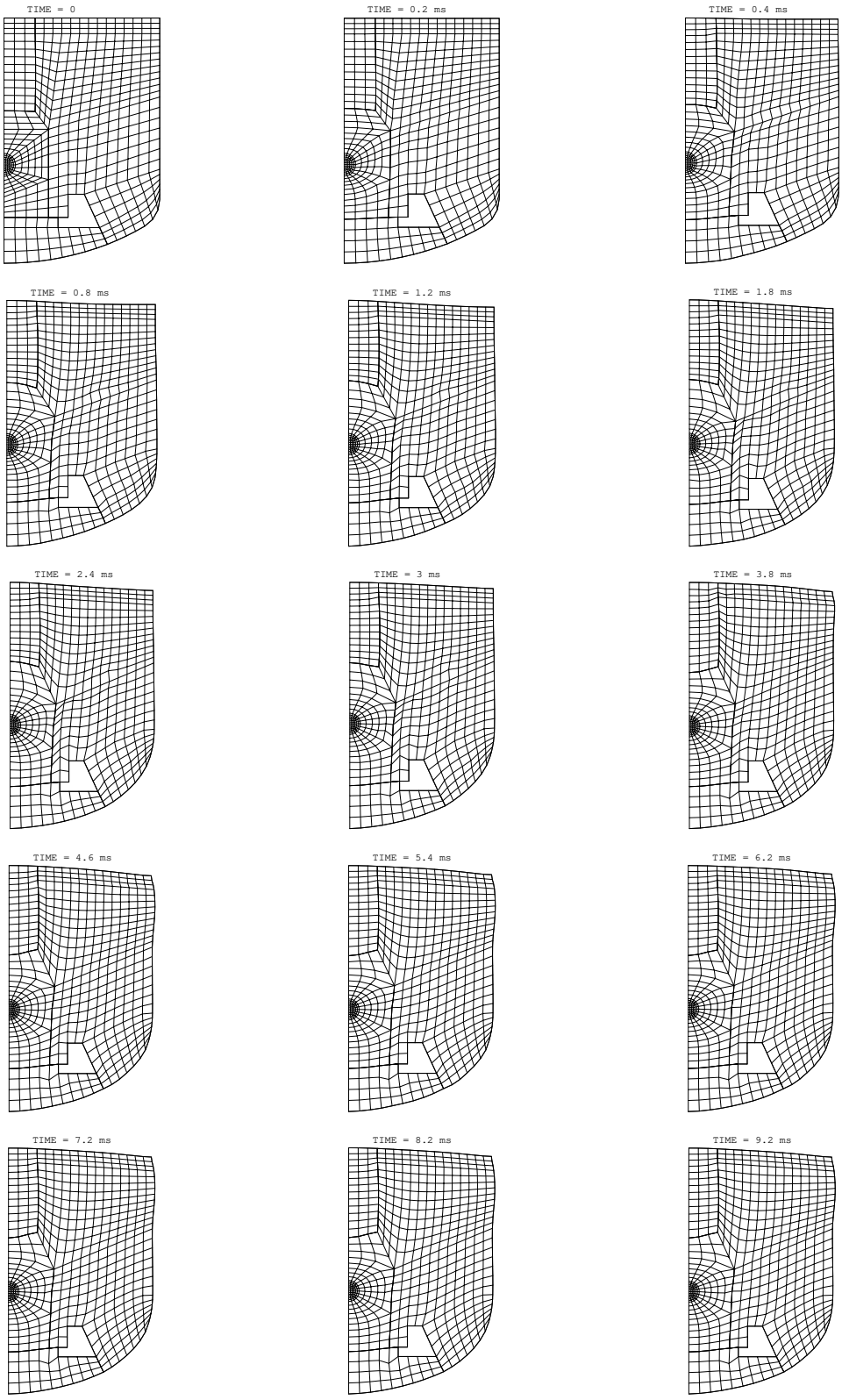

Fig. 10: Deformed shape

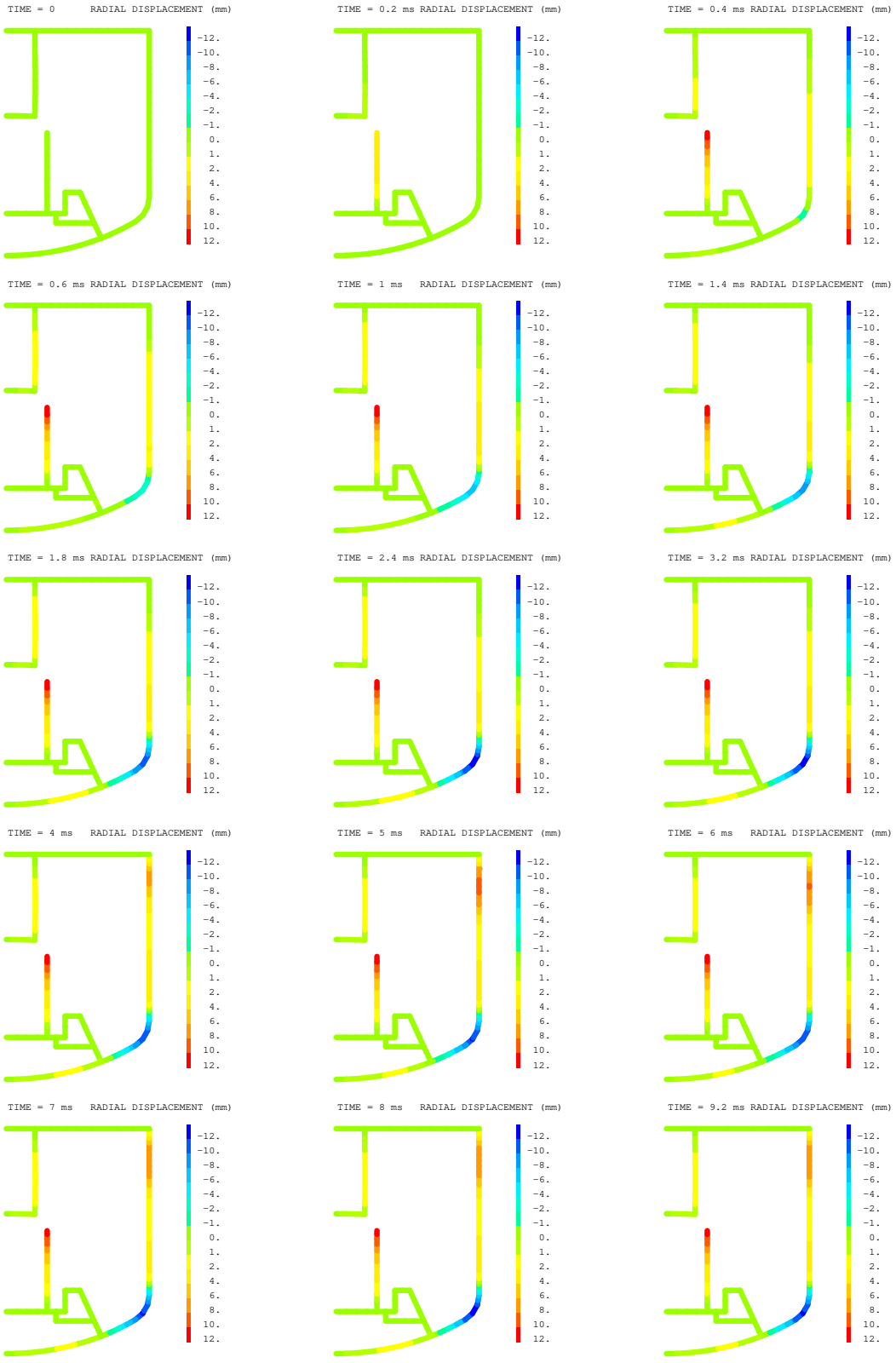

Fig. 11: Radial structure displacements

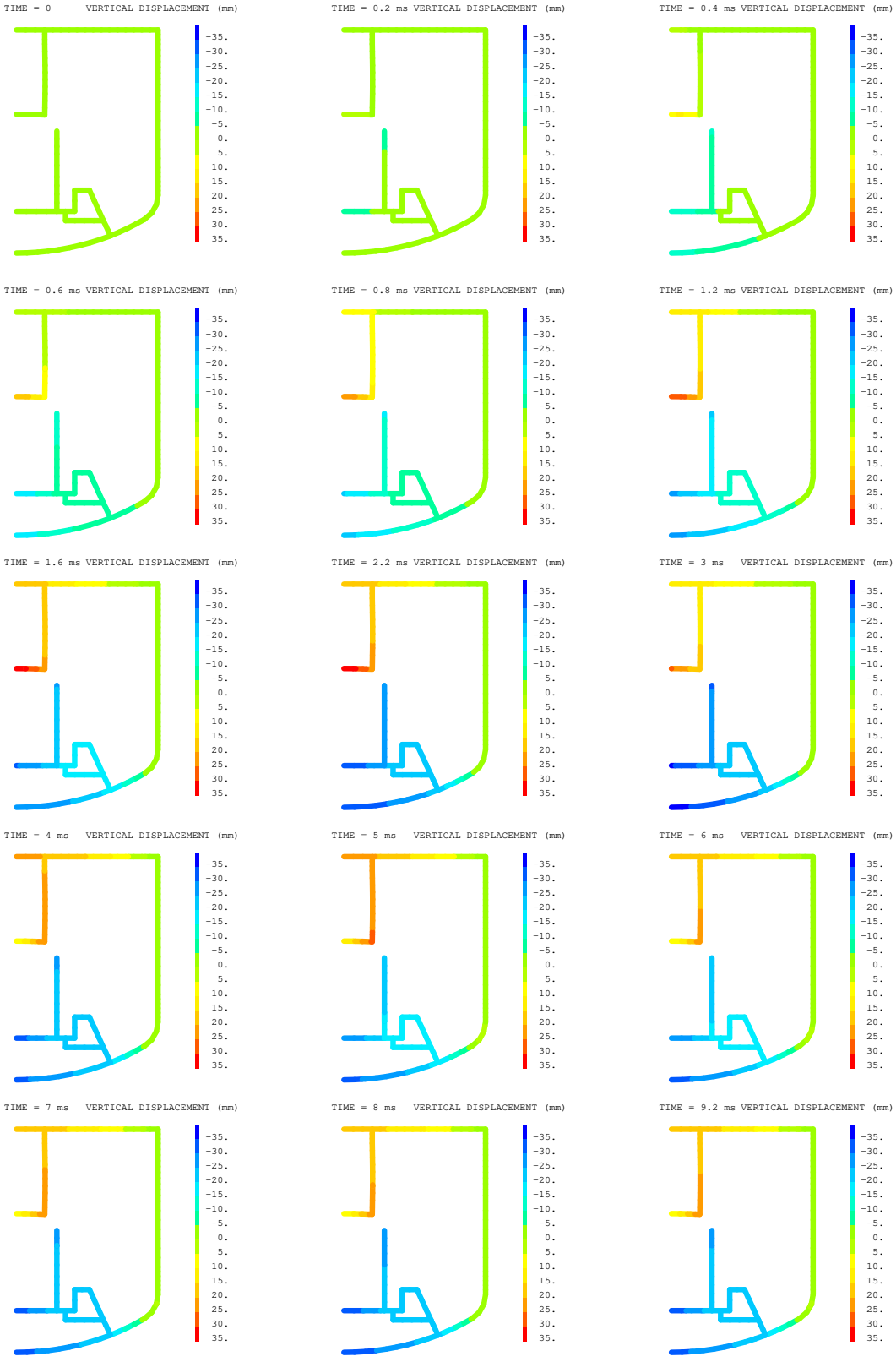

Fig. 12: Vertical structure displacements

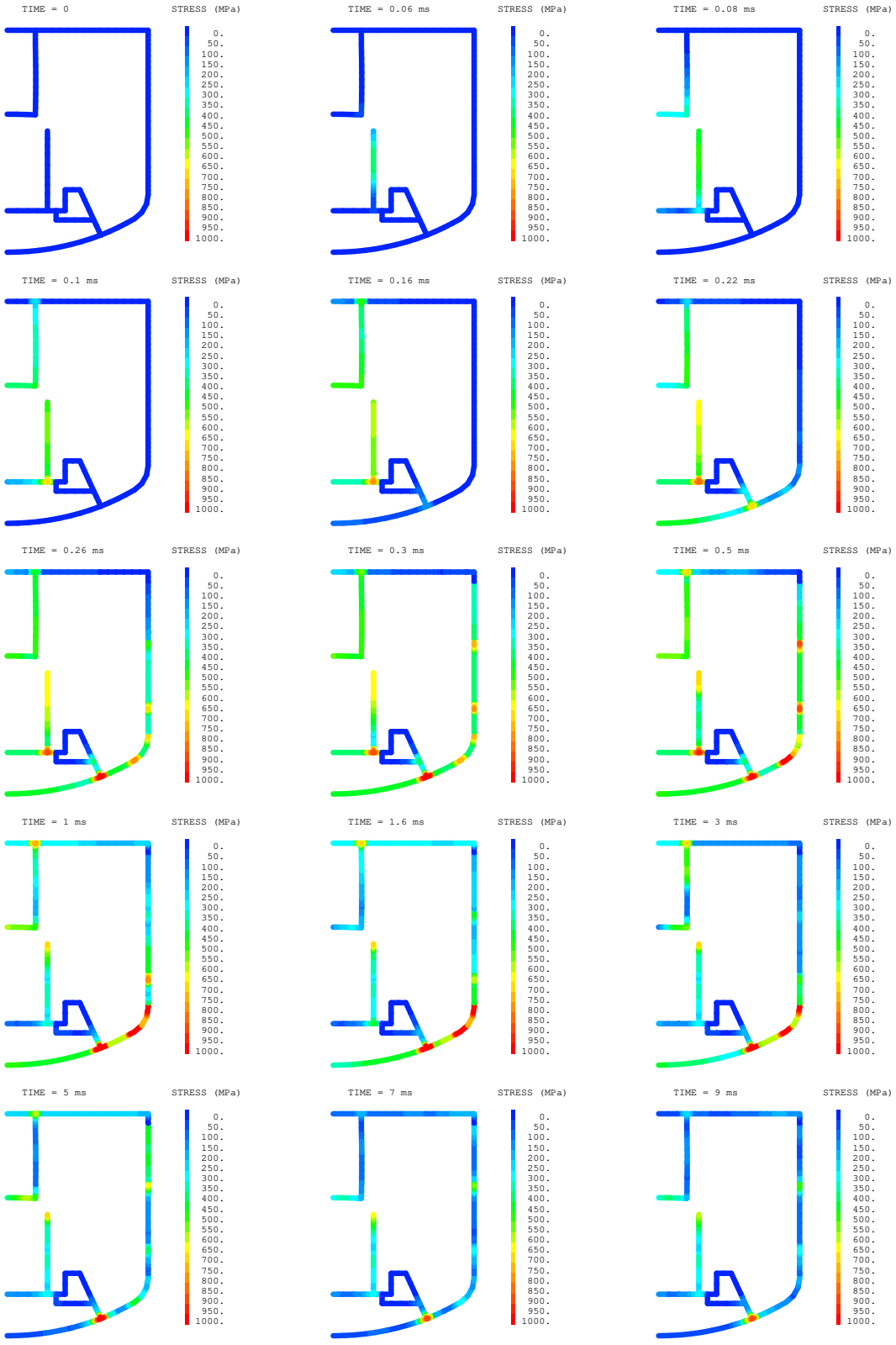

Fig. 13: Von Mises stresses

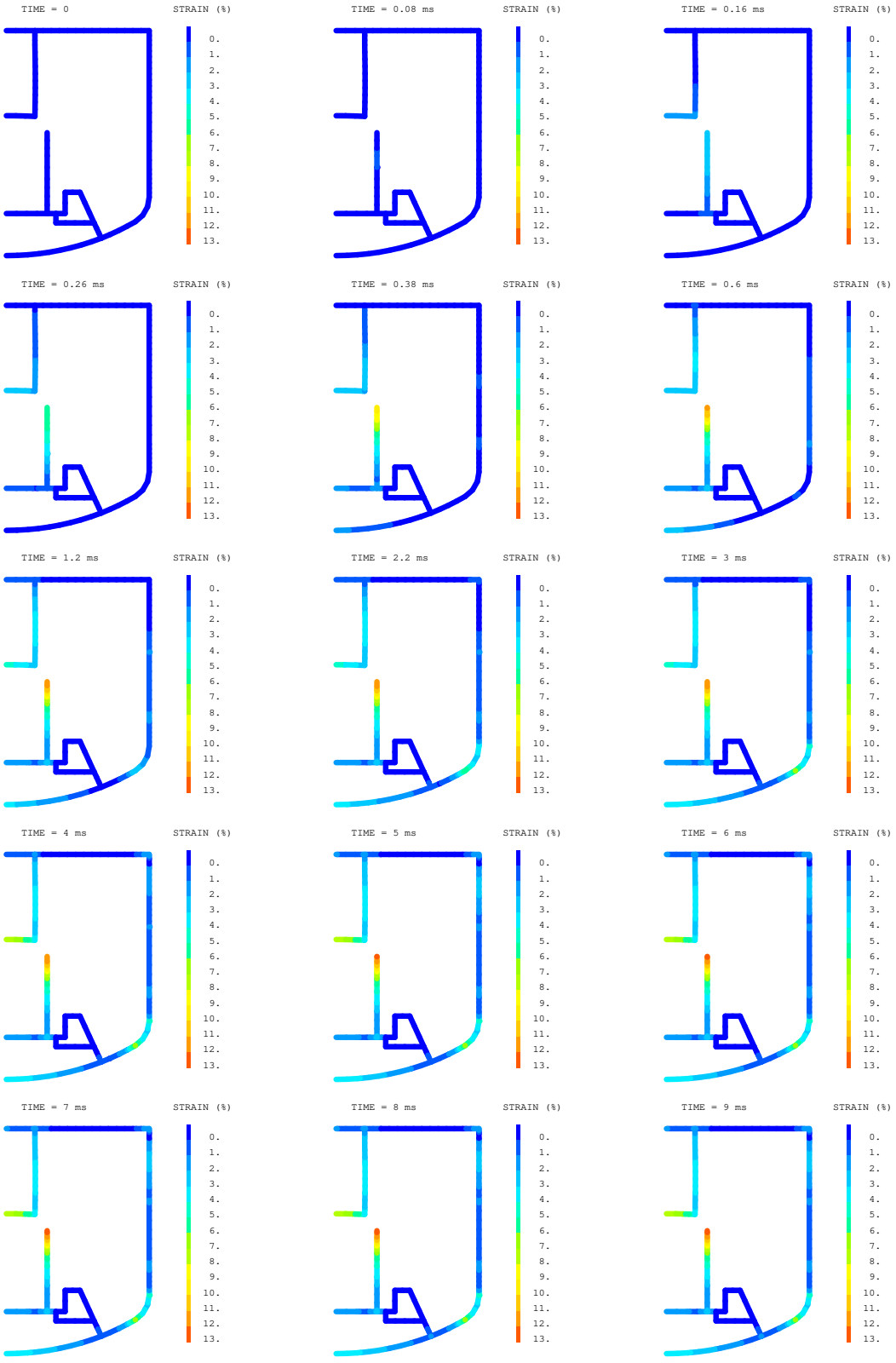

Fig. 14: Plastic strains